Global NEST Journal, Vol 25, No 3, pp 8-16

Removal of BTEX (benzene, toluene, ethyl benzene and xylene) from aqueous solutions using surface-modified zeolite

Saravanan R.[1,*], Sridhar N.[2], Al-Zaqri N.[3], Shalini A.[4], Boshaala A.[5,6], and Gokulan R.[7,*]

[1]Department of Civil Engineering, Kings College of Engineering, Thanjavur 613 303, Tamil Nadu, India

2Department of Civil Engineering, Kongunadu College of Engineering and Technology, Namakkal, Trichy 621 215, Tamil Nadu, India

[3]Department of Chemistry, College of Science, King Saud University, P.O. Box 2455, Riyadh 11451, Saudi Arabia

[4]Department of Civil Engineering, Sona College of Technology, Salem 636 005, Tamil Nadu, India

[5]Research Centre, Manchester Salt & Catalysis, Unit C, 88-90 Chorlton Rd, M154AN Manchester, United Kingdom

[6]Libyan Authority for Scientific Research, P.O. Box 80045, Tripoli, Libya

[7]Department of Civil Engineering, GMR Institute of Technology, Rajam–532 127, Andhra Pradesh, India

Received: 12/12/2022, Accepted: 24/12/2022, Available online: 28/12/2022

*to whom all correspondence should be addressed: e-mail: saravanan.civil@kingsengg.edu.in

https://doi.org/10.30955/gnj.004639

Graphical abstract

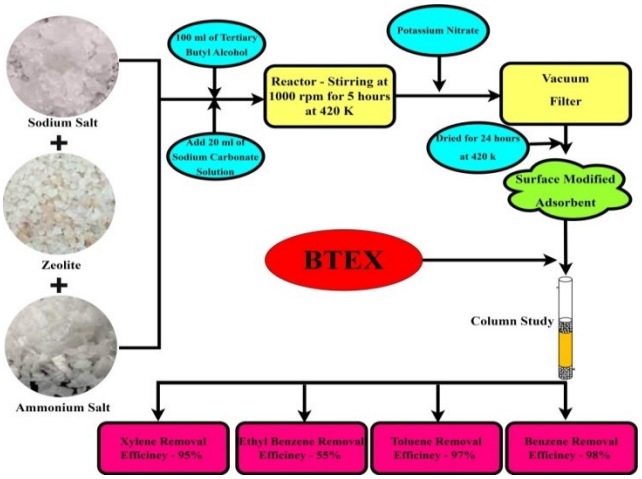

Abstract

BTEX, also known as benzene, toluene, ethyl benzene, and xylene, is a common gasoline oxygenate. The contamination of groundwater and surface water with BTEX and its primary breakdown product has drawn a lot of attention. However, surface-modified zeolite's sorption mechanisms and affinity for BTEX can be employed to potentially remove these toxins from water. Tert-butyl alcohol (TBA) was utilized to alter the morphology of the adsorbent. Based on the findings, it can be concluded that zeolites have a greater capability for removing emerging chemicals. Some of the emerging compounds' relatively large dimensions limit their natural ability to lower values. Gas chromatography was used to determine the BTEX concentration decrease range. The Yoon-Nelson and Adams-Bohart model's use of mathematical modelling to determine the efficacy of the column's adsorption. The model with the highest R^2 values for characterizing equilibrium isotherm data describes equilibrium adsorption data. To gain an understanding of the shape, pore structure, and active sites, the characterisation is concentrated on quantitative analysis using XRD, qualitative analysis using FTIR, and optical study using SEM.

Keywords: BTEX, surface modification, adsorption, characterization

1. Introduction

BTEX volatile organic chemicals, often known as monoaromatic hydrocarbons benzene (B), toluene (T), ethylbenzene (E), and xylene (X), are significant industrial solvents that are regularly found as industrial pollutants (Jiang *et al.,* 2022). According to the structure 6-carbon benzene ring serves as the primary structural component of the mono-aromatic ring compounds benzene, toluene, ethylbenzene, and xylenes. These chemicals, particularly benzene, are typically regarded as non-reactive species due to their closed structures (Zhang *et al.,* 2022). These volatile organic chemicals, which are used to make rubber, printing ink, leather, and gasoline, generate a lot of BTEX-contaminated wastewater that is released into the aquatic environment every year. The World Health Organization (WHO) states that leaks from underground fuel storage tanks into ground water are the most likely cause of BTEX pollution in the environment (Xu *et al.,* 2018). BTEX testing services, the most frequent ways to be exposed to BTEX compounds is by breathing contaminated air, especially in regions near petrol stations, in locations with high levels of automobile traffic, and when smoking cigarettes. Contrary to popular opinion, however, exposure to BTEX from water sources accounts for a very minor portion of daily intake compared to food and breathed air sources (Solovyeva *et al.,* 2018). The BTEX levels in fracking fluids must not be high enough to contaminate drinking water or harm groundwater-dependent plants and animals, according to health and environmental norms. The WHO set Benzene (1ppb), Toluene (180ppb), Ethylbenzene (80ppb), and Xylene as the permitted limits (75 ppb). The BTEX suite of

measurements is helpful (Lenin *et al.,* 2020). There are a lot of VOCs present in normal metropolitan areas, which are given off by everything from paint to car exhaust. BTEX exposure is toxic and has a range of negative effects on human health. According to the classifications, benzene and ethylbenzene are both potentially and carcinogenic to humans (Li *et al.,* 2022). BTEX substances found in drinking water are a sign of significant health hazards that may not be immediately apparent. The primary cause of acute myeloid leukemia is benzene. Long-term exposure to benzene through inhalation can also result in unconsciousness and irritate the eyes and skin. In animal experiments, the evidence indicated that higher concentrations of toluene and xylene were carcinogenic (Liu *et al.,* 2023). The level of BTEX present in the liquid samples can be resolved and determined using a standard GC-MS analysis. There have been reports of numerous ways being used to clean up water that contains BTEX substances (Tang *et al.,* 2022). Adsorption, ozonation, natural attenuation, phytoremediation, and bioremediation are a few of these methods. In a prior work, surface-modified nanotubes were used to adsorb BTEX, and benzene had a higher adsorption capacity than the other three chemicals. This discovery shows that the chemical composition and porosity of the adsorbent surface affect BTEX adsorption by various adsorbents (Zhu *et al.,* 2018). The purpose of this research is to comprehend BTEX adsorption strategies. Tert-butyl alcohol (TBA) was used to modify the surface in order to measure the adsorption capacity of the adsorbent (Wang *et al.,* 2018). Gas chromatographic (GC) analysis was used to measure the removal efficiency. Each unique compound's elution performance was created. The Yoon-Nelson and Adams-Bohart models were used in the Kinetics investigation to confirm the adsorption study's findings. The surface modified adsorbent requires a morphological examination, and this study included quantitative analysis with XRD, qualitative analysis with FTIR, and optical study with SEM. Additionally tested was the adsorbent's ability to regenerate.

2. Materials and methods

2.1. Adsorbate solution

Benzene (Emplura, purity: 98.0%), toluene (Purechems, purity: 98.2%), ethyl benzene (Sigma aldrich: 98%), and xylene (ReAgen, purity: 98%) were the chemicals examined in this study. Using glass gastight microliter syringes, a stock solution of methanol (HamChem, purity: 98.6%-GC) containing 3000 ppm of each of the pollutants was created (Liu *et al.,* 2018). The stock solution was put into a 20 mL glass vial, fitted with a silicone septum and plastic screw cover, sealed with Parafilm, and stored at 100°C in the dark (Shen *et al*., 2022). It was then used every day for a month to produce water solutions with 10 ppm of each of the pollutants. to investigate the effectiveness and capacity of the adsorbent. For the investigation of potential competitive effects in the BTEX-containing water solution developed and applied in kinetics batch experiments.

2.2. Preparation of adsorbent

A quaternary ammonium salt was used to create the zeolite clinoptilolite once it was purchased. By adding sodium salt and tert-butyl alcohol, the initial zeolite was transformed into polycationic zeolite (TBA), Initially, 50.0 g of zeolite and water were mixed to form a dispersion, then 20 mL of a sodium carbonate aqueous solution was added (Yusuff *et al*., 2022). The mixture was put into a glass batch reactor and stirred at a speed of 1000 rpm for five hours at 420K. The Na-saturated zeolite was vacuum filtered after the reaction, rinsed with deionized water to remove extra sodium, and dried for 24 hours at 500K. By using Na+ and TBA at a relative concentration for ion exchange, the surface modified zeolite was created (Mallik *et al*., 2022). The substance was then dried for 24 hours at 420 K, ground to 150 mesh, and made ready for use as an adsorbent.

2.3. Gas chromatography

The GC has been upgraded with an Agilent Technologies 8890 Gas chromatograph (GC) that includes a split/spitless injector, a flame ionization detector (FID), a gas injection valve, and high-pressure regulators. Stainless steel 420L was used for the valves, tubing, ferrules, and nuts (Chen *et al*., 2018). The model utilized has an internal sample loop of 0.10 L and a pressure limit of 1500. The injection valve for gas samples was made by VICI Valco. Helium was used to operate the valves. Using an online liquid injector that could be used at high pressure, liquid samples were injected at a temperature of 100^{o}C (Cai *et al*., 2018). Open capillary tubing with adjustable flow resistance dependent on capillary internal diameter and length was used in the design of split injection. The chromatographic device's hydrodynamic characterization and system validation have been presented (Sun *et al*., 2018). The analysis of light hydrocarbon mixtures in gaseous samples was done in an oven that was heated to a temperature between 50 and 200 degrees Celsius. Methane has been used as a hold up time marker above 500^{o}C to calculate retention factors (below 800^{o}C, methane looked to be marginally retained).

2.4. Adsorption study

A glass column with an internal diameter of 3cm and a length of 90cm was employed for the batch bed column studies (Wang *et al*., 2021). Zeolite that has had its surface changed was used, and its particle sizes ranged from 0.8 mm to 4 mm. Zeolite was used to fill the column, and glass wool was used to cover the bottom. Beds with an 8 cm height were used. The flow rates that were used ranged from 3 to 9ml/min (Mehdi *et al*., 2022). After samples were taken at predefined intervals, IC evaluated the residual BTEX content in the effluent samples (Valdes *et al*., 2021). Column investigations ended when the column neared fatigue. The column studies are carried out at room temperature for practical purposes.

2.4.1. Yoon Nelson model

The Yoon-Nelson Model is more straightforward because it does not call for extensive information regarding the adsorbate (Zou *et al*., 2019). According to this model, the likelihood of adsorption for each adsorbate molecule decreases at a rate that is proportional to both the likelihood of adsorbate adsorption and the likelihood of adsorbate breakthrough on the adsorbent (Gui Y *et al*.,

2019). It is a model for a single component system, the linearized equation of model expressed as Eq:

$$\ln \frac{C_t}{C_o - C_t} = kyt - tky \quad (1)$$

where (min) is the minimum time necessary for 50% adsorbate breakthrough and kyt (min-1) is the rate constant. Model by Yoon and Nelson linear plots. The intercept and slope of the ln [Ct/C0-Ct] vs. t graph's linear plot can be used to derive the parameters ky.

2.4.2. Adams-Bohart model

The Adams Bohart is most frequently used to build fixed bed columns. This model was created on the assumption that intra-particle diffusion and external mass transfer resistance are insignificant factors and that the adsorbate is instantly adsorbed onto the adsorbent surface (Zhang *et al*., 2019). Only the first 10% to 50% of the saturation points, or the breakpoint, of the breakthrough curve are described by this model.

$$\ln\left(\frac{C_t}{C_o}\right) = Kab\,Co\,t - Kab\,Nab\left(\frac{z}{u}\right) \quad (2)$$

The kinetic constant in this equation is written as kab (L/mg min), the linear flow velocity is written as u (cm/min), and the saturation concentration is written as Nab (mg/L) (Saravanan *et al*., 2020). The parameter values for kab and Nab were obtained by plotting the function ln(Ct/C0) versus t and calculating its slope and intercept (Yuan *et al*., 2019). The initial xylene concentration and intake flow rate both altered regarding the kinetic constant kab. Nab's value increased as the initial dye concentration increased. At the start of the electro adsorption process, external diffusion can be the reason for this (Mahmoodi *et al*., 2019). The fact that some data did not fit the model exactly demonstrated its flaws.

2.5. Characterization

2.5.1. X-ray micro-diffraction

The Hard X-ray Micro/Nano-Probe beamline P06 at the storage ring was used for the microprobe experiment, which involved scanning X-ray micro-diffraction measurements and microscopic X-ray fluorescence mapping (Dongguo *et al*., 2018). By using a Kirkpatrick-Baez mirror optic, the beam was concentrated. There were 1800 photons in the focused beam's flux. The thin foil cross-section was positioned using a Keyence optical microscope (Liang *et al*., 2018). XRD signals were captured in transmission geometry using a detector with a 250 mm scintillator screen diameter and an effective pixel size. The samples were aligned using X-ray fluorescence (XRF) signals that were collected using a VORTEX EX Si-drift detector with a 70 mm2 active area (Principe *et al*., 2018). To account for the differences in atomic scattering factors, which are 10 times greater than those of Al, an exposure length of 20 seconds per scan point was selected.

2.5.2. FTIR study

Fourier transform infrared spectroscopy was used to identify the surface species (FT-IR). A Nicolet AVATAR-450 spectrometer was used to capture the FT-IR spectra in KBr pellets. The samples were combined with KBr, dried at 150°C, and then exposed to infrared radiation (Alhassan *et al*., 2020). After processing, the pellets were measured immediately in the mid-infrared region under ambient lighting (Zhang *et al*., 2021). Averaging 35 scans at wavelengths between 6000 and 600 cm^{-1} produced the spectra.

2.5.3. SEM analysis

The material and particle size distribution were graphically described using scanning electron microscope (SEM) equipment (Wang *et al*., 2020). The SIGMA VP analyser was used to run the SEM test. Rheometric Scientific's STA1500 analyser was used to measure the sample mass, which was determined via thermogravimetric analysis (with a constant heating rate) (Yu *et al*., 2019).

2.6. Column regeneration

The column bed was initially washed by DW by upward flow at the same speed as utilized for adsorption from solution in order to regenerate the column for continued usage. The upward flow approach was utilized to pass a 20% NaOH solution at a flow rate of 1.50 mL/min (Wang *et al*., 2019). The concentration of collected wastewater was measured (Xin *et al*., 2019). After the desorption cycle, the column bed was cleaned with distilled water until the pH of the effluent was neutral. In order to test the reusability of the adsorbent, the cleaned column was utilized once more for the subsequent adsorption cycle, which was followed up by the subsequent three adsorption cycles (Yongchao *et al*., 2021).

3. Result and discussion

3.1. BTEX adsorption study

BTEX examined each compound's adsorption capacity in order to determine which compound best exhibited the adsorbent's ability to remove impurities and standardize the adsorbent for that compound.

3.2. Benzene removal

Batch process experiments were used to study benzene adsorption. For the benzene elimination experiment, a sample was taken every 10 minutes, and gas chromatography was utilized to determine how well the therapy was working. The first round of treatment study included 8 cm-diameter surface-modified adsorbent columns. The intake sample level was 2.5 mL/min in 8 cm, whereas the outflow ranges were 0.7 mL/min. The column reached saturation with a concentration of 0.084 mg/L in 130 minutes, and the Kinetics graph showed R^2= 0.9893, indicating a removal efficiency of 98% within the first hour of treatment (Cheng *et al*., 2021). According to the graph, benzene adsorption began during the first ten minutes and had a progressive, linear removal concen-tration before the column became saturated at a concen-tration of around 0.084 mg/L (Figures 1–4 and Tables 1–5).

Table 1 Benzene Removal Concentration

Time (min)	8 cm column (mg/L)
0	0.850
10	0.773

20	0.745
30	0.661
40	0.612
50	0.544
60	0.501
70	0.437
80	0.379
90	0.316
100	0.253
110	0.101
120	0.084
130	0.084

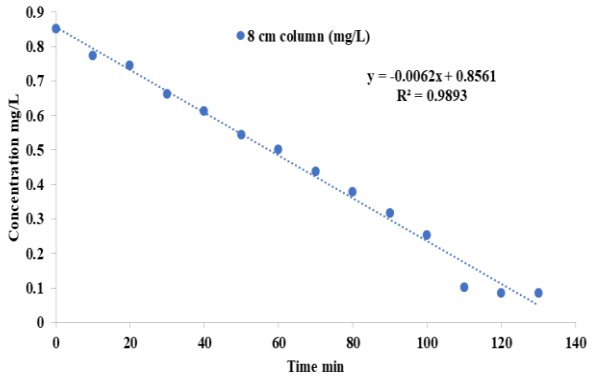

Figure 1. Benzene Removal Efficiency

3.3. Toluene removal

Batch process experimentation was used to research toluene adsorption. A sample was taken for the benzene exclusion examination every ten minutes, and Gas chromatography was employed to judge how well the behaviour was working. Surface-modified adsorbent columns with an 8 cm diameter were employed in the initial action investigation. The sample levels for the in-take were 2.5 mL/min in 8 cm, whereas the output ranges were 0.7 mL/min. The column was saturated at an atten-tiveness of 0.062 mg/L after 180 minutes, and the treatment efficacy during the first hour varied from 0.850 mg/L. The kinetics graph showed an R^2 value of 0.9876, indicating a 97% removal efficiency. According to the graph, the toluene adsorption process began within the first 10 minutes and developed linearly until the column became saturated at a concentration of around 0.062 mg/L (Ahmad *et al*., 2021).

3.4. Ethyl benzene

Batch process studies were used to observed the adsorption of ethyl benzene. A sample was engaged for the benzene removal examination every ten minutes, and Gas chromatography was utilized to critic how well the treatment was working. Surface-modified adsorbent columns with an 8 cm diameter were hired in the initial treatment investigation. The sample levels for the intake were 2.5 mL/min in 8 cm, whereas the output ranges were 0.7 mL/min. Treatment efficiency peaked at 0.850 mg/L during the first hour, then dropped to 0.437 mg/L after 120 minutes. The Kinetics graph showed an R^2 value of 0.9641, indicating a 55% amputation efficiency. According to the graph, ethyl benzene adsorption began during the first ten minutes and had a slow and linear removal concentration before the column became saturated at a concentration of around 0.437 mg/L. When compared to other chemicals, the surface modification is not as suitable for ethyl benzene (Seftel *et al*., 2018).

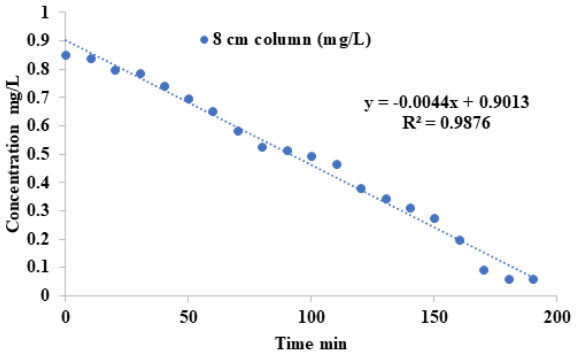

Figure 2. Toluene Removal Efficiency

Table 2. Toluene Removal Concentration

Time (min)	8 cm column (mg/L)
0	0.850
10	0.841
20	0.801
30	0.784
40	0.743
50	0.697
60	0.651
70	0.584
80	0.526
90	0.513
100	0.497
110	0.464
120	0.382
130	0.346
140	0.312
150	0.274
160	0.199
170	0.093
180	0.062
190	0.062

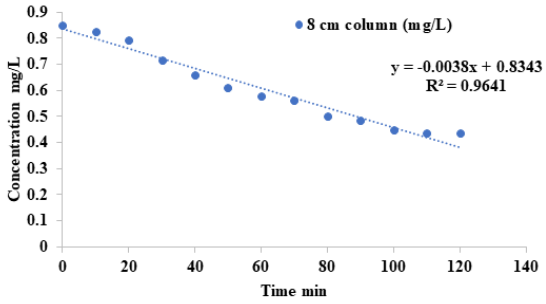

Figure 3. Ethyl Benzene Removal Efficiency

Table 3. Ethyl Benzene Removal Concentration

Time (min)	8 cm column (mg/L)
0	0.850
10	0.826
20	0.794
30	0.715

40	0.661
50	0.610
60	0.578
70	0.563
80	0.501
90	0.487
100	0.449
110	0.437
120	0.437

3.5. Xylene

Utilizing batch process investigations, xylene adsorption was studied. For the benzene elimination experiment, a sample was taken every 10 minutes, and gas chromatography was utilized to determine how well the therapy was working. The first round of treatment study included 8 cm-diameter surface-modified adsorbent columns. The intake sample level was 2.5 mL/min in 8 cm, whereas the outflow ranges were 0.7 mL/min. The column was saturated with a concentration of 0.072 mg/L after 160 minutes, and the treatment effectiveness during the first hour varied from 0.850 mg/L. The R^2 value on the Kinetics graph revealed a 95% removal efficiency (Li *et al*., 2018). According to the graph, the column became saturated in the range of 0.072 mg/L after the xylene adsorption began in the first ten minutes and had a slow and linear elimination concentration.

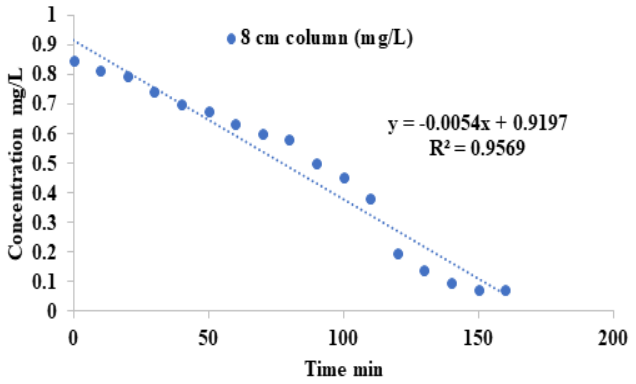

Figure 4. Xylene Removal Efficiency

3.6. Gas chromatographic analysis (GC)

After the adsorption research, the samples were gathered and put in vials that were maintained in the fridge in order to observe the chromatogram. Through the mobile phase and stationary phase, a 20µl sample that was injected into the intake region. when determining the ideal level was done using the gas chromatography result graph (Touzeau *et al*., 2018). GC was utilized to measure the BTEX level after the graphical representation analysed by software. The peak's height and area were used to compute the sample's BTEX content based on the graphical representation. The graph from the GC revealed that better removal was achieved for (A) Benzene, (B) Toluene, and 55% removal for Ethyl Benzene, which is shown in the pictorial representation as (C) Ethyl Benzene. Normal removal was also achieved for Xylene, but only very minor traces were found in the graph, which was represented as (D) Xylene. The interaction between the BTEX chemical and the surface-modified zeolite adsorbent was revealed by all ranges (Xu *et al*., 2019). Figure 5 shown that, aside from Ethyl Benzene, the adsorbent is suitable for the other three compounds.

Table 4. Xylene Removal Concentration

Time (min)	8 cm column (mg/L)
0	0.850
10	0.813
20	0.795
30	0.742
40	0.703
50	0.678
60	0.634
70	0.599
80	0.581
90	0.502
100	0.454
110	0.383
120	0.196
130	0.142
140	0.098
150	0.072
160	0.072

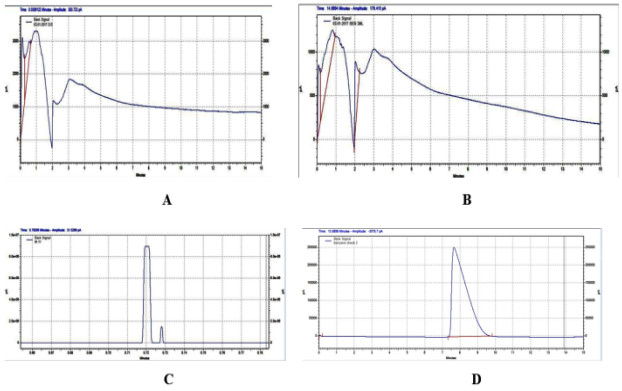

Figure 5. Determination of BTEX Removal by Gas Chromatography (A) Benzene, (B) Toluene, (C) Ethyl Benzene, (D) Xylene

3.7. Kinetic study

3.7.1. Yoon Nelson model

Based on the values of the regression coefficients, the Yoon-Nelson model confirmed that it was compatible with surface-modified adsorbents. The results showed that benzene had a stronger adsorption break through with an R^2 value greater than 0.9861, toluene had an R^2 value of 0.9752, ethyl benzene had an R^2 value of 0.9626, and xylene had an R2 value of 0.9563. The rate constant values in the row of BTEX were 2.63, 2.30, 1.64, and 2.04 respectively. For BTEX, the Ky(min^{-1}) are 0.582, 0.513, 0.323, and 0.497 (Janus *et al*., 2019). This said that the experimental results were nearly entirely determined by the kinetic values of BTEX elimination (Figures 6 and 7).

Table 5. BTEX removal study by Yoon – nelson model

Materials	Column Height (cm)	Ky(min^{-1})	τ(hr)	R2
Benzene	8	0.582	2.63	0.9861
Toluene	8	0.513	2.30	0.9752
Ethyl Benzene	8	0.323	1.64	0.9626
Xylene	8	0.497	2.04	0.9563

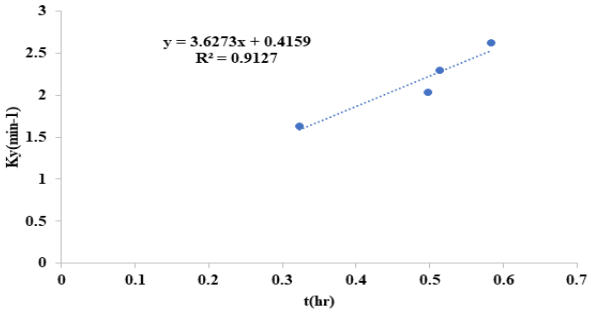

Figure 6. Yoon Nelson Model Kinetic study for BTEX

3.7.2. Adams-Bohart model

The kinetic constant Kab was affected by the starting concentration, bed height, and inflow flow rate, respectively. The adsorption capability of BTEX is justified by Nab's value at greater starting solvent concentrations. At the start of the electro adsorption process, external diffusion can be the reason for this. The values for R^2, *K*ab, and *N*ab are shown in Table 6. Not every number fit the model, exposing its shortcomings (Deluo *et al*., 2019). This created constant, however, supports the Yoon Nelson model, which already supports the real-time adsorption trials.

Table 6. Adams-Bohart model for BTEX adsorption

Material	Column size (cm)	Nab (mg/L)	Kab (ml/mg min)	R2
Benzene	8	463.14	0.0057	0.9823
Toluene	8	412.76	0.0043	0.9701
Ethyl Benzene	8	258.35	0.0029	0.9614
Xylene	8	399.27	0.0048	0.9531

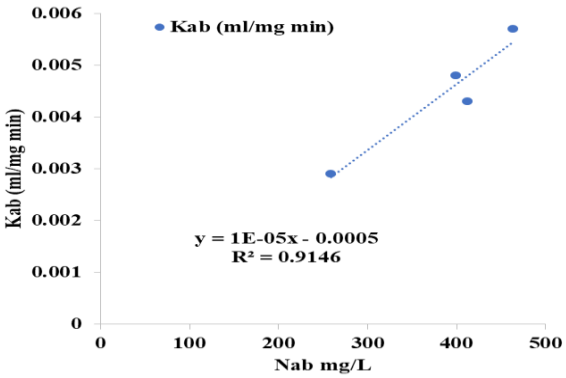

Figure 7. Adams-Bohart Model Kinetic study for BTEX

3.8. Characterisation

3.8.1. X-ray micro-diffraction for BTEX adsorption

The structure of the single crystal would be distorted by the mutual slip of the tightly packed macromolecular chains along the D-axis. One of the most popular techniques for characterizing crystal structures in powdered materials is XRD. It has been suggested that XRD can also be used to understand characteristics like crystallite sizes and geometries. In the current investigation, XRD measurements were used to track the irreversible crystalline deformation. An XRD pattern of the emulsion polymerized material (E1) is shown in Figure 8. According to the phase IV's hexagonal symmetry, all the peaks that formed can be classified. The adsorbent particles produced by the emulsion polymerization have a distinctive structure where each particle is made up of tightly folded ribbon-like crystals. The structural periodicities along axes perpendicular to the D-axis are unaffected by the deformation. The situation with the pyramidal lattice planes is very different. Glide distances along the shear direction at the various slip planes are unequal during the deformation process (Figure 8). As a result, structural regularities along the normal of the pyramidal planes are significantly reduced (Niu *et al*., 2019). The diffraction peaks 210 and 220 are significantly stronger than the others, and changes in their strength can be used to gauge the extent of crystal deformation.

3.8.2. FTIR study for BTEX adsorption

Adsorbent FTIR- spectra analysed statistically, and the results showed that axis 1, axis 3, and axis 3 together accounted for 81.3%, 20.14%, and 8.1% of the variability, respectively (Figure 9). On both axes 1 and, the adsorbent displayed a substantial separation (P 0.0005). According to Tukey's post hoc analysis, one adsorbent substantially differed from another along axis 1. On the third axis, A greatly diverged from axis one in a positive direction, and Tv significantly diverged from a different angle in a negative direction. There were five significant and two important peaks for species D, four significant and one important peak for species S, and two important peaks for species R analysis of the x-residuals acquired from the species that had previously been chosen by the analysis on axis 1. Peaks at 3142, 1428, and 2748 in the average IR spectrum of species S are present but absent in the average spectra of other species (Ma *et al.,* 2019). Axis 1 accounted for 72% of the variability, axis 2 for 25%, and axis 3 for 70% as a result of the adsorbent (Figure 9)

3.8.3. SEM analysis for BTEX adsorption

According to the thorough adsorption analysis, BTEX seem green to turquoise. Surface modification affects how the solutions look in terms of hue. The off-white TBA material has always undergone the colour of flakes appear in brown after the adsorption studies. The adsorption model must be better understood in order to determine the cause of colour variations. Figure 10 depicts the SEM picture of the pure and TBA surface modified adsorbent, which was used to characterize the TBA samples for this purpose. A rough, uneven surface is what we see. As can be seen from the colour change in the SEM pictures of the TBA surface after BTEX adsorption, the surface structure greatly varies depending on the initial BTEX concentration. The

completer and more developed the crystal-like structure generated, the higher the BTEX concentration at which it occurs, the occurrence of crystal-like structures on the adsorbent surface. This could be the reason for how the variation in light refraction at the surface causes the intensity of the black colour of the adsorbent flakes with higher initial salt concentration to fluctuate (Raghav *et al*., 2018). The crystal-led TBA modified adsorbent structure was confirmed by EDX analysis to be the consequence of the adsorption of both ions.

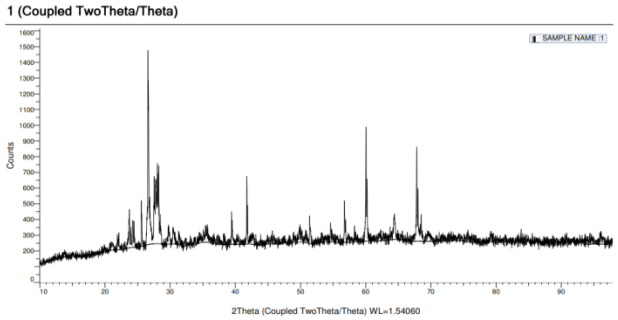

Figure 8. X-ray micro-diffraction for BTEX

3.9. Regeneration of adsorbent

The cleaned column was used once more for the succeeding adsorption cycle, which was followed by the following three adsorption cycles, in order to assess the adsorbent's reusability. The adsorbent was repackaged and used brand-newly once again to assess its reusability. which translates to three study cycles (Yu-Jung *et al*., 2018). After the third cycle, the TBA component's surface modification loosened the link between the zeolite adsorbent and TBA. This demonstrated how BTEX removal varied.

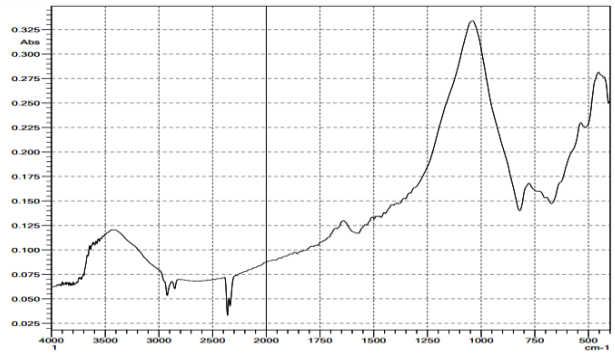

Figure 9. FTIR study for BTEX

4. Conclusion

Zeolite nanoparticles were synthesized by Tert Butyl Alcohol (TBA) to produce surface modified adsorbent. The prepared adsorbent used as an adsorbent for the adsorption removal of BTEX from aqueous solution. This adsorbent study exhibits as a result of Benzene 98%, Toluene 97%, Ethyl Benzene 55%, and Xylene 95%. The surface nature of TBA had slight variation in Ethyl Benzene so the removal attained only 55%. Due to physical and chemical properties the TBA initially interaction well with Benzene, Toluene and Xylene. Kinetic studies showed that the adsorption followed the Yoon Nelson Model and Adams-Bohart model Equilibrium isotherm data were fitted well with the experimental adsorption isotherm and physical adsorption process. The surface modification proved that the removal efficiency enhanced by the corporeal changes in adsorbent. The regeneration was achieved for three cycle of adsorption treatment. In initial stage of adsorption process should be controlled mainly by diffusion. The removal of BTEX can be improved through enhancing agitation.

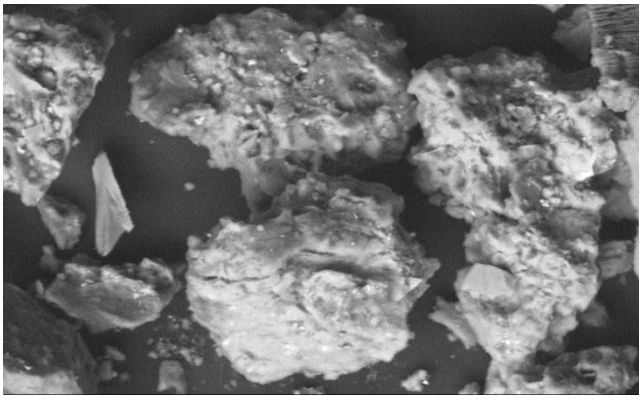

Figure 10. SEM Analysis for BTEX

Conflict of Interest

The authors declare no conflict of interest

Acknowledgement

The authors are grateful to GMR Institute of Technology, Rajam Andhra Pradesh for providing facilities for the conduct of laboratory Investigations. The authors extend their appreciation to the Researchers Supporting Project number (RSP2023R396), King Saud University, Riyadh, Saudi Arabia.

Reference

Mallik A.K., Md. Abdul Moktadir, Md. Ashiqur Rahman, Md. Shahruzzaman, and Rahman M.M. (2022). Progress in surface-modified silicas for Cr(VI) adsorption: A review. *Journal of Hazardous materials*, **423**, 127041.

Yusuff A.S., Popoola L.T., and Igbafe A.I. (2022). Response surface modeling and optimization of hexavalent chromium adsorption onto eucalyptus tree bark-derived pristine and chemically-modified biochar. *Chemical Engineering Research and Design*, **182**, 59220–603.

Cai W., Li Z., Wei J., and Liu Y. (2018). Synthesis of peanut shell based magnetic activated carbon with excellent adsorption performance towards electroplating wastewater, *Chemical Engineering Research and Design*, **140**,.23–32.

Chen F., Zhu Q., Li S., Xu Z., Sun X., and Zhao S. (2018). The function of poly aromatic nuclei structure for adsorption of vanadyl/nickel etioporphyrin on asphaltene/graphene. *Fuel Processing Technology*, **174**, 132–141.

Cheng Q., Zhang Y., Zheng X., Sun W., Bo Tao Li., Wang D., and Li Z. (2021). High specific surface crown ether modified chitosan nanofiber membrane by low-temperature phase separation for efficient selective adsorption of lithium. *Separation and Purification Technology*, **262**, 118312.

Niu F.F., Cai M., Pang J., Li X., Yang D., and Zhang G. (2019). Gas molecular adsorption effects on the electronic and optical properties of monolayer SnP3. *Vacuum*, **168**, 108823.

Gang D.J., Xiaolai L., Changqiao Z., and Yuan Z.S. (2019). Adsorption of C5Pe molecules on silica surfaces with different

hydrophobicity studied by molecular dynamics simulation. *Applied surface Science*, **495**, 143624.

Gui Y., Chen J., Wang W., Zhu Y., Tang C., and Xu L. (2019). Adsorption mechanism of hydrogen sulfide and sulfur dioxide on Au–MoS2 monolayer, Superlattices and Microstructures, **135**, 106280.

Principe I.A., Murdoch B., Flannigan J.M., Fletcher A.J. (2018). Decoupling microporosity and nitrogen content to optimize CO2 adsorption in melamine–resorcinol–formaldehyde xerogels. Materialstoday Chemistry, **10**, 195–205.

Janus R., Wadrzyk M., Natkanski P., Cool P., and PiotrKuStowski. (2019). Dynamic adsorption–desorption of methyl ethyl ketone on MCM-41 and SBA-15 decorated with thermally activated polymers, *Journal of Industrial and Engineering Chemistry*, **71**, 465–480.

Jiang C., Yue F., Li C., Zhou S., and Zheng L. (2022). Polyethyleneimine-modified lobster shell biochar for the efficient removal of copper ions in aqueous solution: Response surface method optimization and adsorption mechanism. *Journal of Environmental Chemical Engineering*, **10**, 108996.

Dongguo L., Chung Hoon T., Maurya S., Matanovic I., and Seung K.Y. (2018). Impact of ionomer adsorption on alkaline hydrogen oxidation activity and fuel cell performance. *Current opinion in Electrochemistry*, **12**, 189–195.

Li G., Xue B., He X., Chen T., and Wei X. (2022). Superhydrophobic Surface-modified zeolite to regulate the migration of nonadsorbed liquid water in an Open-loop adsorption heat pump. *Applied Thermal Engineering*, **215**, 118929.

Li H., Kang J., Zhaou F., Qiang Z., and Li G. (2018). Adsorption heat features of coalbed methane based on microcalorimeter. *Journal of Loss Prevention in the Process Industry*, **55**, 37–449.

Liang Y-t., Han J.-W., Chen-bing A.L., and Qin W.-q. (2018). Adsorption and leaching behaviors of chalcopyrite by two extreme thermophilic archaea, Transactions of Nonferrous metals Society of China, **28**, 2538–2544.

Liu J., Xiong J., Ju X., BoGao, Wang L., and Sillanpaa M. (2018). Streaming potential for identification of foulants adsorption on PVDF membrane surface. *Journal of Membrane Science*, **566**, 428–434.

Liu Y., Wei Z., Hu X., and Zi F. (2023). Flotation performance and adsorption mechanism of sodium lauroyl sarcosinate on lead ion-modified bastnaesite surfaces, *Minerals Engineering*, **191**, 107960.

Lenin M., Sunda A., Aravindan S., Sujatha S., Mahendran G., Kalyani D., Zunaithur Rahman A., Vijayakumar M., Senthil Kumar. (2020). Biochar derived from Caulerpa scalpelliformis for the removal of Reactive Yellow 81 in batch and packed bed column. *Biomass Conversion and Biorefinery*, 2020.

Ma C., Jin W., Ma X., HanHan, Yu J., and Wu Y. (2019). Water adsorption behaviors of high index polar surfaces in ZnO. *Applied surface science*, **498**, 143898.

Mahmoodi M.N., Mohsen A.T., Taghizadeh, Zim M.A., and Baglou S. (2019). Surface modified montmorillonite with cationic surfactants: Preparation, characterization, and dye adsorption from aqueous solution. *Journal of Environmental Chemical Engineering*, **7**, 103243.

Mehdi B., Belkacemi H., Brahmi-ingrachen D., Braham L.A., and Mehr L. (2022). Study of nickel adsorption on NaCl-modified natural zeolite using response surface methodology and kinetics modelling. *Groundwater for sustainable development*, **17**, 100757.

Ahmad M.B., Soomro U., Muqeet M., and Ahmed Z. (2021). Adsorption of Indigo Carmine dye onto the surface-modified adsorbent prepared from municipal waste and simulation using deep neural network. *Journal of Hazardous Materials*, **408**, 124433.

Sapna, Raghav S., Nair M., and Dinesh Kumar. (2018). Trimetallic oxide entrapped in alginate polymeric matrix employed for adsorption studies of fluoride. *Surfaces and Interfaces*, **13**, 112–132.

Saravanan A., Karishma S., Jeevanantam S., Jeyasri S., and Kiruthika A.R. (2020). Optimization and modeling of reactive yellow adsorption by surface modified Delonix regia seed: Study of nonlinear isotherm and kinetic parameters, *Surfaces and Interfaces*, **20**, 100520.

Seftel E.M., Ciocarlan R.G., Michielsen B., Meynen V., Mullens S., and Cool P. (2018). Insights into phosphate adsorption behavior on structurally modified ZnAl layered double hydroxides. *Applied Clay Sciences*, 165, 234–246.

Shen X., Wang H., Zhao Y. Liang J., Lu B., Sun W., Lu K., Wang H., Yuan L. (2022). Recycling protein selective adsorption on fluorine-modified surface through fluorine-fluorine interaction, Colloids and surfaces B: Bio interfaces, **214**, 112486.

Alhassan S.I., He Y., Huang L., Wu B., Yan L., Deng H., Wang H. (2020). A review on fluoride adsorption using modified bauxite: Surface modification and sorption mechanisms perspectives. *Journal of Environmental Chemical Engineering*, **8**, 104532.

Solovyeva M.V., GordeevaL.G., Kriger T.A., and Aristow Yu.I. (2018). MOF-801 as a cooling: equilibrium and dynamics of water adsorption. *Energy conversion and Management*, **174**, 356–363.

Sun W., Yue D., Song J., and Nie Y. (2018). Adsorption removal of refractory organic matter in bio-treated municipal solid waste landfill leachate by anion exchange resins, *Waste Management*, **81**, 61–70.

Tang X., Zhang H., Sun C., Qiao X., and Ju D. (2022). Adsorption mechanisms over ZrO_2-modified Cu(1 1 1) surface for X (CH_3OH, H_2O and CO): A DFT+U Study, *Surface Science*, **716**, 121976.

Touzeau J., Barbault F., Maurel F., and Seydou M. (2018). Insights on porphyrin-functionalized graphene: Theoretical study of substituent and metal-center effects on adsorption. *Chemical Physics letters,* **713**, 172–179.

Valdes H., Riqelme A.L., Solar V.A., Azzolina-Jury F., and Thibault-Starzyk F. (2021). Removal of chlorinated volatile organic compounds onto natural and Cu-modified zeolite: The role of chemical surface characteristics in the adsorption mechanism. *Separation and Purification Technology*, **258**, 118080.

Wang C., Liu R., Wu M, Zhai Q., Sun W., Jing N., and Xie F. (2021). Induced adsorption of pectin on copper-ion-modified galena surfaces: Flotation and adsorption mechanism. *Minerals Engineering*, **173**, 107229.

Wang Y., Du T., Qiu J.Z., and Song Y. (2018). Synthesis, characterization and CO_2 adsorption of NaA, NaX and NaZSM-5 from rice husk ash. *Solid State Science*, **86**, 24–33.

Wang Y., Jia T.D., Qiu Z., and Song Y. (2019). Effect of extra-framework cation in ion-exchanged ZSM-5 from

rice husk ash on CO_2 adsorption. *Solid state sciences* **97**, 105985.

Wang Z., Mahmood A., Xie X., Wang X., Qiu H., and Sun J. (2020). Surface adsorption configurations of H_3PO_4 modified TiO_2 and its influence on the photodegradation intermediates of gaseous o-xylene. *Chemical Engineering Journal*, **393**, 124723.

Xin F., Xu H., Tang D., and Cao L. (2019). Properties of lignite and key factors determining the methane adsorption capacity of lignite: New insights into the effects of interlayer spacing on adsorption capacity. *Fuel Processing Technology*, **196**, 106181.

Xu W., Chen Y., Zhang W., and Li B. (2019). Fabrication of graphene oxide/bentonite composites with excellent adsorption performances for toluidine blue removal from aqueous solution, *Advanced Powder Technology*, **30**, 493–501.

Xu W., Lou Y., Xu B., Li Y., Zhao Y., Xiong, and Jing J. (2018). Mineralized calcium carbonate/xanthan gum microspheres for lysozyme adsorption. *international journal of Biological Macromolecules*, **120**, 2175–2179.

Yongchao, Shuming M., Qicheng W., and Liao R.F. (2021). Enhanced adsorption of salicylhydroxamic acid on ilmenite surfaces modified by Fenton and its effect on floatability, *Colloids and Surfaces A: Physicochemical and Engineering Aspects*, **626**, 127057.

Yu W., Xu H., Roden E.E., and Wan Q. (2019). Efficient adsorption of iodide from water by chrysotile bundles with wedge-shaped nanopores, *Applied Clay Sciences*, **183**, 105331.

Yuan J., Amano Y., and Machida M. (2019). Surface modified mechanism of activated carbon fibers by thermal chemical vapor deposition and nitrate adsorption characteristics in aqueous solution. Colloids and surfaces A: *Physicochemical and Engineering Aspects*, **580**, 123710.

Yu-Jung L., Wen-Zhi C., Ting O., SooraMohan, and Chang-Tang C. (2018). Adsorption mechanism of magnetic nanoparticles doped with graphene oxide and titanium nanotubes for As(III) removal. *Materialia*, **3**, 79201–89.

Zhang D., Zhang K., Hu X., He Q., Yani J., and Xue Y. (2021). Cadmium removal by $MgCl_2$ modified biochar derived from crayfish shell waste: Batch adsorption, response surface analysis and fixed bed filtration. *Journal of Hazardous Materials*, **408**, 124860.

Zhang L., Jian G., Puerto M., Southwick E., Hirasaki G., and Biswal S.L. (2019). Static adsorption of a switchable diamine surfactant on natural and synthetic minerals for high-salinity carbonate reservoirs. *Colloids and surfaces B: Physicochemical and Engineering Aspects*, **583**, 123910.

Zhang S., Xian Y., Wen S., and Liang G. (2022). Enhancement of xanthate adsorption on lead-modified and sulfurized smithsonite surface in the presence of ammonia. Minerals Engineering, **189**, 107872.

Zhu H., Xiao X., Guo Z., Han X., Liang Y., Zhang Y., and Zhou C. (2018). Adsorption of vanadium (V) on natural kaolinite and montmorillonite: Characteristics and mechanism. *Applied Clay Science*, **161**, 310–316.

Zou J., Rezaee R., Xie Q., and You L. (2019). Characterization of the combined effect of high temperature and moisture on methane adsorption in shale gas reservoirs. *Journal of Petroleum Science and Engineering*, **182**, 106353.